

# Constraints on quasi-normal-mode frequencies with LIGO-Virgo binary-black-hole observations

Abhirup Ghosh,<sup>1</sup> Richard Brito,<sup>2</sup> and Alessandra Buonanno<sup>1,3</sup>

<sup>1</sup>*Max Planck Institute for Gravitational Physics (Albert Einstein Institute), Am Mühlenberg 1, Potsdam 14476, Germany*

<sup>2</sup>*Dipartimento di Fisica, “Sapienza” Università di Roma & Sezione INFN Roma1, Piazzale Aldo Moro 5, 00185 Roma, Italia*

<sup>3</sup>*Department of Physics, University of Maryland, College Park, MD 20742, USA*

(Dated: April 1, 2021)

The no-hair conjecture in General Relativity (GR) states that the properties of an astrophysical Kerr black hole (BH) are completely described by its mass and spin. As a consequence, the complex quasi-normal-mode (QNM) frequencies of a binary-black-hole (BBH) ringdown can be uniquely determined by the mass and spin of the remnant object. Conversely, measurement of the QNM frequencies could be an independent test of the no-hair conjecture. This paper extends to spinning BHs earlier work that proposed to test the no-hair conjecture by measuring the complex QNM frequencies of a BBH ringdown using parameterized inspiral-merger-ringdown waveforms in the effective-one-body formalism, thereby taking full advantage of the entire signal power and removing dependency on the predicted or estimated start time of the ringdown. Our method was used to analyze the properties of the merger remnants for BBHs observed by LIGO-Virgo in the first half of their third observing (O3a) run. After testing our method with GR and non-GR synthetic-signal injections in Gaussian noise, we analyze, for the first time, two BBHs from the first (O1) and second (O2) LIGO-Virgo observing runs, and two additional BBHs from the O3a run. We then provide joint constraints with published results from the O3a run. In the most agnostic and conservative scenario where we combine the information from different events using a hierarchical approach, we obtain, at 90% credibility, that the fractional deviations in the frequency (damping time) of the dominant QNM are  $\delta f_{220} = 0.03^{+0.10}_{-0.09}$  ( $\delta \tau_{220} = 0.10^{+0.44}_{-0.39}$ ), respectively, an improvement of a factor of  $\sim 4$  ( $\sim 2$ ) over the results obtained with our model in the LIGO-Virgo publication. The single-event most-stringent constraint to date continues to be GW150914 for which we obtain  $\delta f_{220} = 0.05^{+0.11}_{-0.07}$  and  $\delta \tau_{220} = 0.07^{+0.26}_{-0.23}$ .

## I. INTRODUCTION

The LIGO Scientific Collaboration [1] and the Virgo Collaboration [2] have recently announced their catalogue of gravitational-wave (GW) signals from the first half of the third observing run (O3a) [3]. Combined with the first and second observing-run catalogues [4], the Advanced LIGO detectors at Hanford, Washington and Livingston, Louisiana [5], and the Advanced Virgo detector in Cascina, Italy [6] have now detected 50 GW events from the merger of compact objects like neutron stars and/or black holes (BHs). Alongside independent claims of detections [7–10], these results have firmly established the field of GW astronomy, five years after the first detection of a GW passing through Earth, GW150914 [11].

The observation of GWs has had significant astrophysical and cosmological implications [12–15]. It has also allowed us to probe fundamental physics and test predictions of Einstein’s theory of General Relativity (GR) in the previously unexplored highly-dynamical, and strong field regime [16–19]. In GR, a binary black hole (BBH) system is described by three distinct phases: an early *inspiral* [20], where the two compact objects spiral in loosing energy because of the emission of GWs, a *merger* [21–23] marked by the formation of a common apparent horizon, and a *ringdown* [24–28], during which the newly formed remnant object settles down to a Kerr BH emitting quasi-normal-modes (QNMs) (i.e., damped oscillations with specific, discrete frequencies and decay times).

The LIGO-Virgo collaborations have released companion papers detailing their results of tests of GR for GW150914 [16], and for several GW events of the two transient catalogues (TC): GWTC-1 [4, 18] and GWTC-2 [3, 19]. The results include tests of GW generation and source dynamics,

where bounds are placed on parameterized deviations in the post-Newtonian (PN) coefficients describing the early inspiral, and phenomenological coefficients describing the intermediate (plunge) and merger regimes of coalescence [17, 29–31]; tests of GW propagation, which assume a generalized dispersion relation and place upper bounds on the Compton wavelength and, consequently, the mass of the graviton [32, 33], and tests of the polarization of gravitational radiation using a multi-GW-detector network [34, 35]. The GWTC-1/2 papers also check for consistency between different portions of the signal using estimates for the predicted mass and spin of the remnant object [16, 36, 37], and consistency of the residuals with detector noise [18, 38]. None of these tests report any departure from the predictions of GR.

The first paper on tests of GR by the LIGO Collaboration [16] also provided us with the first measurement of the dominant damped-oscillation signal in the ringdown stage of a BBH coalescence, and more recently a similar measurement was made with the high-mass event GW190521 [39, 40]. The set of available measurements was greatly expanded in the latest LIGO-Virgo O3a testing GR paper [19] where a comprehensive analysis of the properties of the remnant object, including the ringdown stage, was reported for tens of GW events. The no-hair conjecture in GR [41–45] states that an (electrically neutral) astrophysical BH is completely described by two observables: mass and spin. One consequence of the no-hair conjecture is that the (complex) QNM frequencies of gravitational radiation emitted by a perturbed isolated BH are uniquely determined by its mass and spin. Hence a test of the no-hair conjecture would involve checking for consistency between estimates of mass and spin of the remnant object across multiple QNM frequencies [46, 47]. An incon-

sistency would either indicate a non-BH nature of the remnant object, or an incompleteness of GR as the underlying theory of gravity.

The consistency between the post-merger signal and the least damped QNM was first demonstrated in Ref. [16] for GW150914, and confirmed through several independent analyses [48–51]. This was later extended to include overtones in Refs. [19, 50, 52]. Consistency of the late-time waveform with a single QNM is a test of the ringdown of a BBH coalescence, but not necessarily a test of the no-hair conjecture, which requires the measurement of (at least) two QNMs (BH spectroscopy), and consistency between them [46, 50, 53–59]. The nature of the remnant object has also been explored through tests of BH thermodynamics, including the Hawking’s area theorem [60, 61], the Bekenstein-Hod universal bound [62], the BH area quantization [63, 64], the consistency of the merger frequency with predictions from NR simulations [56] or through search for echos in the post-merger signal [65–70]. None of these tests have found evidence for non-BH nature of the remnant object (as described in GR) in LIGO-Virgo BBH observations.

Ground-based detectors, such as LIGO and Virgo, are most sensitive to stellar-mass BH binaries that form remnants with mass  $\gtrsim 50M_{\odot}$  and merge near the minimum of their sensitivity band ( $\sim 100$  Hz). As a consequence, the remnant object *rings down* at frequencies where the sensitivity is worse, leaving very little signal-to-noise ratio (SNR) in the post-merger signal. Most of the tests mentioned above restrict the data to this post-merger signal which, while being agnostic to deviations in the pre-merger dynamics, significantly reduces parameter-estimation capabilities. Added to a lack of SNR is the ambiguity in clearly defining a start time for the ringdown phase (discussed, for example, in Refs. [71–73]). In some tests [49, 56], the ringdown start time has been left as a free parameter to be estimated directly from the data. Whereas, in other cases, the ringdown start time is predicted from corresponding full-signal parameter-estimation analyses (see pyRing analysis in Ref. [19]). Uncertainties in estimates of the ringdown start time, as well as an overall lack of SNR in the post-merger signal, given typical sensitivities of ground-based detectors, can result in significant statistical uncertainties in the measurement of some of the QNM properties. This is especially true for the measurement of the QNM damping times which are, in general, harder to measure from the data. Hence, one might want to look at alternate methods to measure QNMs using information from as much as the signal as possible.

An independent approach to BH spectroscopy, based on the full-signal analysis, was introduced in Ref. [48] (henceforth referred to as Paper I). Unlike methods that focus only on the post-merger signal, it employs the complete inspiral-merger-ringdown (IMR) waveform to measure the complex QNM frequencies. In the current version, this method assumes that GR provides a very good description of the signal up to merger, while being agnostic about the complex QNM frequencies. This allows to access the full SNR of the signal, reducing measurement uncertainties. However, we note that this method can incorporate deviations from GR, notably from the (known) PN coefficients, also during the long in-

spiral stage [17–19], and can in principle incorporate deviations from GR, notably from the parameters calibrated to NR simulations, in the late inspiral and plunge. Moreover, in this method, the definition of the ringdown start time is built into the merger-ringdown model and does not need to be either left as an additional free parameter or fixed using alternate definitions. While Paper I presented the method and tested it for non-spinning BBHs, here we extend the analysis to the more realistic astrophysical case in which BHs carry spin. Furthermore, the IMR waveform model used in this paper is more accurate than what employed in Paper I, because it contains higher-order corrections in PN theory and it was calibrated to a much larger set of numerical-relativity (NR) waveforms [74]. All astrophysical BHs are expected to be spinning, and ignoring effects of spin has been shown to introduce systematic biases in the measurement of the source properties.

The rest of the paper is organized as follows. Section II A describes our parameterized IMR waveform model. In Sec. II B, we define our framework to test GR, notably how we can measure complex QNM frequencies with our parameterized model within a Bayesian formalism, and validate it using several synthetic-signal injection studies in Gaussian noise in Sec. III. Then, in Sec. IV, we apply our method on real GW events in LIGO and Virgo data. In particular, we analyze the GWTC-2 events and obtain the most stringent constraints on the dominant (complex) QNM frequencies. Finally, in Sec. V we provide a summary of our results and discuss future developments.

## II. WAVEFORM MODEL AND STATISTICAL STRATEGY TO MEASURE QUASI-NORMAL MODES

A GW signal from the (quasi-circular) coalescence of two BHs is completely described in GR by 15 parameters,  $\xi_{\text{GR}}$ . These can be grouped into the *intrinsic* parameters: the (source) masses,  $m_1, m_2$  and spins,  $\vec{S}_1, \vec{S}_2$  of the component objects in the binary; and the *extrinsic* parameters: a reference time  $t_c$  and phase  $\phi_c$ , the sky position of the binary  $(\alpha, \delta)$ , the luminosity distance,  $d_L$ , and the binary’s orientation described through the inclination of the binary  $i$  and its polarization  $\psi$ . We also introduce the total (source) mass  $M = m_1 + m_2$ , and the (dimensionless) symmetric mass ratio  $v = m_1 m_2 / M^2$ . We also follow the convention  $m_1 > m_2$ , and hence the asymmetric mass ratio,  $q = m_1 / m_2 \geq 1$ . We also introduce the detector masses  $m_{1\text{det}} = (1+z)m_1$  and  $m_{2\text{det}} = (1+z)m_2$ , where  $z$  is the redshift.

Here, we focus on BHs with spins aligned or anti-aligned with the orbital angular momentum (henceforth, aligned-spin). In this case, the GW signal depends on 11 parameters. We denote the aligned-spin (dimensionless) components as  $\chi_i = |\vec{S}_i|/m_i^2$ , where  $i = 1, 2$  for the two BHs.

### A. Parameterized waveform model

As in Paper I, we use an IMR waveform model developed within the effective-one-body (EOB) formalism [75, 76]. However, whereas Paper I was limited to non-spinning multipolar waveforms, here we use as our baseline model the aligned-spin multipolar waveform model developed in Ref. [77]. In addition to being calibrated to NR simulations, this model also uses information from BH perturbation theory for the merger and ringdown phases. Henceforth we will denote this model by SEOBNR for short<sup>1</sup>.

In the observer's frame, the GW polarizations can be written as

$$h_+(\iota, \varphi_0; t) - i h_\times(\iota, \varphi_0; t) = \sum_{\ell, m} {}_{-2}Y_{\ell m}(\iota, \varphi_0) h_{\ell m}(t), \quad (2.1)$$

where  $\varphi_0$  is the azimuthal direction to the observer (note that without loss of generality we can take  $\phi_c \equiv \varphi_0$ ), while  ${}_{-2}Y_{\ell m}(\iota, \varphi_0)$  are the  $-2$  spin-weighted spherical harmonics. The SEOBNR model we employ includes the  $(\ell, |m|) = (2, 2), (2, 1), (3, 3), (4, 4)$ , and  $(5, 5)$  modes [77]. For each  $(\ell, m)$ , the inspiral-(plunge-)merger-ringdown SEOBNR waveform is schematically given by

$$h_{\ell m}(t) = h_{\ell m}^{\text{inspiral-plunge}} \theta(t_{\text{match}}^{\ell m} - t) + h_{\ell m}^{\text{merger-RD}} \theta(t - t_{\text{match}}^{\ell m}), \quad (2.2)$$

where  $\theta(t)$  is the Heaviside step function,  $h_{\ell m}^{\text{inspiral-plunge}}$  represents the inspiral-plunge part of the waveform, whereas  $h_{\ell m}^{\text{merger-RD}}$  denotes the merger-ringdown waveform, which reads [74, 77]

$$h_{\ell m}^{\text{merger-RD}}(t) = \nu \tilde{A}_{\ell m}(t) e^{i\tilde{\phi}_{\ell m}(t)} e^{-i\sigma_{\ell m 0}(t-t_{\text{match}}^{\ell m})}, \quad (2.3)$$

where  $\nu$  is the symmetric mass ratio of the binary and  $\sigma_{\ell m 0} = 2\pi f_{\ell m 0} - i/\tau_{\ell m 0}$  denotes the complex frequency of the fundamental QNMs of the remnant BH. We denote the oscillation frequencies by  $f_{\ell m 0} \equiv \Re(\sigma_{\ell m 0})/(2\pi)$  and the decay times by  $\tau_{\ell m 0} \equiv -1/\Im(\sigma_{\ell m 0})$ . The functions  $\tilde{A}_{\ell m}(t)$  and  $\tilde{\phi}_{\ell m}(t)$  are given by [74, 77]:

$$\tilde{A}_{\ell m}(t) = c_{1,c}^{\ell m} \tanh[c_{1,f}^{\ell m}(t - t_{\text{match}}^{\ell m}) + c_{2,f}^{\ell m}] + c_{2,c}^{\ell m}, \quad (2.4a)$$

$$\tilde{\phi}_{\ell m}(t) = \phi_{\text{match}}^{\ell m} - d_{1,c}^{\ell m} \log \left[ \frac{1 + d_{2,f}^{\ell m} e^{-d_{1,f}^{\ell m}(t-t_{\text{match}}^{\ell m})}}{1 + d_{2,f}^{\ell m}} \right], \quad (2.4b)$$

where  $\phi_{\text{match}}^{\ell m}$  is the phase of the inspiral-plunge mode  $(\ell, m)$  computed at  $t = t_{\text{match}}^{\ell m}$ . The coefficients  $d_{1,c}^{\ell m}$  and  $c_{i,c}^{\ell m}$  with  $i = 1, 2$  are fixed by imposing that the functions  $\tilde{A}_{\ell m}(t)$  and  $\tilde{\phi}_{\ell m}(t)$  are of class  $C^1$  at  $t = t_{\text{match}}^{\ell m}$ , when matching the merger-ringdown waveform to the inspiral-plunge SEOBNR waveform  $h_{\ell m}^{\text{inspiral-plunge}}(t)$ . This allows us to write the coefficients  $c_{i,c}^{\ell m}$

as [77]:

$$c_{1,c}^{\ell m} = \frac{1}{c_{1,f}^{\ell m} \nu} [\partial_t |h_{\ell m}^{\text{inspiral-plunge}}(t_{\text{match}}^{\ell m})| - \sigma_{\ell m}^{\text{R}} |h_{\ell m}^{\text{inspiral-plunge}}(t_{\text{match}}^{\ell m})|] \cosh^2(c_{2,f}^{\ell m}), \quad (2.5a)$$

$$c_{2,c}^{\ell m} = -\frac{|h_{\ell m}^{\text{inspiral-plunge}}(t_{\text{match}}^{\ell m})|}{\nu} + \frac{1}{c_{1,f}^{\ell m} \nu} [\partial_t |h_{\ell m}^{\text{inspiral-plunge}}(t_{\text{match}}^{\ell m})| - \sigma_{\ell m}^{\text{R}} |h_{\ell m}^{\text{inspiral-plunge}}(t_{\text{match}}^{\ell m})|] \cosh(c_{2,f}^{\ell m}) \sinh(c_{2,f}^{\ell m}), \quad (2.5b)$$

and  $d_{1,c}^{\ell m}$  as

$$d_{1,c}^{\ell m} = [\omega_{\ell m}^{\text{inspiral-plunge}}(t_{\text{match}}^{\ell m}) - \sigma_{\ell m}^{\text{I}}] \frac{1 + d_{2,f}^{\ell m}}{d_{1,f}^{\ell m} d_{2,f}^{\ell m}}, \quad (2.6)$$

where we denoted  $\sigma_{\ell m}^{\text{R}} \equiv \Im(\sigma_{\ell m 0}) < 0$  and  $\sigma_{\ell m}^{\text{I}} \equiv -\Re(\sigma_{\ell m 0})$ , and  $\omega_{\ell m}^{\text{inspiral-plunge}}(t)$  is the frequency of the inspiral-plunge EOB mode. The coefficients  $c_{i,f}^{\ell m}$  and  $d_{i,f}^{\ell m}$  are obtained through fits to NR and Teukolsky-equation-based waveforms and can be found in Appendix C of Ref. [77].

In the SEOBNR model constructed in Ref. [77], the complex frequencies  $\sigma_{\ell m 0}$  are expressed in terms of the final BH mass and spin [47, 78], and the latter are related to the BBH's component masses and spins through NR-fitting-formulas obtained in GR [79, 80]. Here instead, in the spirit of what was done in Paper I, we promote the QNM (complex) frequencies to be free parameters of the model, while keeping the inspiral-plunge modes  $h_{\ell m}^{\text{inspiral-plunge}}(t)$  fixed to their GR values. More explicitly, we introduce a parameterized version of the SEOBNR model where the frequency and the damping time of the  $\ell m 0$  mode (i.e.,  $(f_{\ell m 0}, \tau_{\ell m 0})$ ) are defined through the fractional deviations,  $(\delta f_{\ell m 0}, \delta \tau_{\ell m 0})$ , from the corresponding GR values [53, 54].

Thus,

$$f_{\ell m 0} = f_{\ell m 0}^{\text{GR}} (1 + \delta f_{\ell m 0}), \quad (2.7a)$$

$$\tau_{\ell m 0} = \tau_{\ell m 0}^{\text{GR}} (1 + \delta \tau_{\ell m 0}). \quad (2.7b)$$

The GR quantities  $(f_{\ell m 0}^{\text{GR}}, \tau_{\ell m 0}^{\text{GR}})$  are constructed using the NR-fitting-formula from Refs. [79, 80], and are functions of the initial masses and spins,  $(m_1, m_2, \chi_1, \chi_2)$ . Hence,

$$f_{\ell m 0} = f_{\ell m 0}(m_1, m_2, \chi_1, \chi_2, \delta f_{\ell m 0}, \delta \tau_{\ell m 0}), \quad (2.8a)$$

$$\tau_{\ell m 0} = \tau_{\ell m 0}(m_1, m_2, \chi_1, \chi_2, \delta f_{\ell m 0}, \delta \tau_{\ell m 0}). \quad (2.8b)$$

We denote such a parameterized waveform model pSEOBNR<sup>2</sup>. We note that when leaving  $\sigma_{\ell m}$  to vary freely, the functions  $\tilde{A}_{\ell m}(t)$  and  $\tilde{\phi}_{\ell m}(t)$  in general also differ from the GR predictions, since those functions depend on the QNM complex frequencies, as can be seen from the expressions for  $c_{i,c}^{\ell m}$  and  $d_{i,c}^{\ell m}$  in Eqs. (2.5a), (2.5b), and (2.6). As a consequence, the ringdown signal (amplitude and phase) soon after merger deviates from the one predicted by GR.

<sup>1</sup>In the LIGO Algorithm Library (LAL), this waveform model is called SEOBNRv4HM.

<sup>2</sup>This waveform model is called pSEOBNRv4HM in LAL.

## B. Bayesian parameter-estimation technique

The parameterized model, pSEOBNR, described above introduces an additional set of non-GR parameters,  $\xi_{\text{nGR}} = (\delta f_{\ell m 0}, \delta \tau_{\ell m 0})$ , corresponding to each  $(\ell, m)$  QNM present in the GR waveform model SEOBNR. One then proceeds to use the Bayes' theorem to obtain the *posterior* probability distribution on  $\lambda = \{\xi_{\text{GR}}, \xi_{\text{nGR}}\}$ , given a hypothesis  $\mathcal{H}$ :

$$P(\lambda|d, \mathcal{H}) = \frac{P(\lambda|\mathcal{H}) \mathcal{L}(d|\lambda, \mathcal{H})}{P(d|\mathcal{H})}, \quad (2.9)$$

where  $P(\lambda|\mathcal{H})$  is the *prior* probability distribution, and  $\mathcal{L}(d|\lambda, \mathcal{H})$  is called the *likelihood* function. The denominator is a normalization constant  $P(d|\mathcal{H}) = \int P(\lambda|\mathcal{H}) \mathcal{L}(d|\lambda, \mathcal{H}) d\lambda$ , called the marginal likelihood, or the *evidence* of the hypothesis  $\mathcal{H}$ . In this case, our hypothesis  $\mathcal{H}$  is that the data contains a GW signal that is described by the pSEOBNR waveform model  $h(\lambda)$  and stationary Gaussian noise described by a power spectral density (PSD)  $S_n(f)$ . The likelihood function can consequently be defined as:

$$\mathcal{L}(d|\lambda, \mathcal{H}) \propto \exp \left[ -\frac{1}{2} \langle d - h(\lambda) | d - h(\lambda) \rangle \right], \quad (2.10)$$

where  $\langle . | . \rangle$  is the usual noise-weighted inner product:

$$\langle A | B \rangle = \int_{f_{\text{low}}}^{f_{\text{high}}} df \frac{\tilde{A}^*(f) \tilde{B}(f) + \tilde{A}(f) \tilde{B}^*(f)}{S_n(f)}. \quad (2.11)$$

The quantity  $\tilde{A}(f)$  denotes the Fourier transform of  $A(t)$  and the  $*$  indicates complex conjugation. The limits of integration  $f_{\text{low}}$  and  $f_{\text{high}}$  define the bandwidth of the sensitivity of the GW detector. We usually assume  $f_{\text{high}}$  to be the Nyquist frequency whereas  $f_{\text{low}}$  is dictated by the performance of the GW detector at low-frequency. Here, we follow the choice made in the LIGO-Virgo analysis [3, 4]. Owing to the large dimensionality of the parameter set  $\lambda$ , the posterior distribution  $P(\lambda|d, \mathcal{H})$  in Eq. (2.9) is computed by stochastically sampling the parameter space using techniques such as Markov-chain Monte Carlo (MCMC) [81, 82] or Nested Sampling [83]. For this paper, we use the LALInference [84] and Bilby codes [85–87] that provide an implementation of the parallelly tempered MCMC and Nested Sampling algorithms respectively, for computing the posterior distributions.

Given the full-dimensional posterior probability density function  $P(\lambda|d, \mathcal{H})$ , we can marginalize over the *nuisance* parameters, to obtain the marginalized posterior probability density function over the QNM parameters  $\xi_{\text{nGR}}$ :

$$P(\xi_{\text{nGR}}|d, \mathcal{H}) = \int P(\lambda|d, \mathcal{H}) d\xi_{\text{GR}}. \quad (2.12)$$

For most of the results discussed in this paper, we restrict ourselves to the  $(\ell m) = (2, 2)$  and/or  $(3, 3)$  modes. In those cases we assume  $\xi_{\text{nGR}} = \{\delta f_{220}, \delta \tau_{220}\}$  and/or  $\{\delta f_{330}, \delta \tau_{330}\}$ , and fix all the other  $(\ell m)$  modes to their GR predictions (i.e.,  $\delta f_{\ell m 0} = \delta \tau_{\ell m 0} = 0$ ). This is because, for most of the high-mass BH events that we find most appropriate for this test, the

LIGO-Virgo observations are consistent with nearly-equal-mass face-on/off BBHs for which power in the subdominant modes is not enough to attempt to measure more than one QNM complex frequency.

Lastly, throughout our analysis, we assume uniform priors on our non-GR QNM parameters,  $(\delta f_{\ell m 0}, \delta \tau_{\ell m 0})$ . We note that since the priors on  $(f_{\ell m 0}^{\text{GR}}, \tau_{\ell m 0}^{\text{GR}})$  are derived through NR-fits, from the corresponding priors on the initial masses and spins, this leads to a non-trivial prior on the final reconstructed frequency and damping time,  $(f_{\ell m 0}, \tau_{\ell m 0})$ . Also, given the definition of the damping time in Sec. II A, we note that  $\delta \tau_{\ell m 0} = -1$  leads to the imaginary part of the QNM complex frequency going to infinity. We avoid this by restricting the minimum of the prior on  $\delta \tau_{\ell m 0}$  to be greater than  $-1$ .

## III. SYNTHETIC-SIGNAL INJECTION STUDY

### A. Simulations using GR signals in Gaussian noise

We now demonstrate our method using synthetic-signal injections describing GWs from BBHs in GR. We employ coloured Gaussian noise with PSDs for LIGO and Virgo detectors during the fourth observing (O4) run [88], which is expected to start in the second half of 2022 [6, 89]. For the mock BBH signals, we choose parameters similar to two specific GW events, GW150914 [11] and GW190521 [39]. We list them in Table I. These two binary systems are representative of the kind of systems for which the QNM measurement is most suitable, notably high-mass BBH events which are loud enough that the pre- and post-merger SNRs return reliable parameter-estimation results.

| Injection     | Network | $m_1^{\text{det}}$<br>( $M_\odot$ ) | $m_2^{\text{det}}$<br>( $M_\odot$ ) | $\chi_1$ | $\chi_2$ | $\rho_{\text{IMR}}$ | $\rho_{\text{insp}}$ | $\rho_{\text{postinsp}}$ |
|---------------|---------|-------------------------------------|-------------------------------------|----------|----------|---------------------|----------------------|--------------------------|
| GW150914-like | HL      | 39                                  | 31                                  | 0.0      | 0.0      | 25                  | 22                   | 12                       |
| GW190521-like | HL      | 150                                 | 120                                 | 0.02     | -0.39    | 20                  | 8                    | 18                       |
| SXS:BBH:0166  | HLV     | 72                                  | 12                                  | 0.0      | 0.0      | 71                  | 58                   | 41                       |

TABLE I. Parameters of the synthetic-signal injections, chosen to be similar to the actual GW events indicated in the first column (first two rows). The parameters ( $m_1^{\text{det}}, m_2^{\text{det}}$ ) are the detector-frame masses of the primary and secondary BHs, respectively. The third row indicates the parameters of the SXS BBH waveform used in Sec. III C. The second column refers to the detector-network used, with H,L,V, referring to LIGO-Hanford, LIGO-Livingston and Virgo, respectively. The quantities  $\rho_{\text{IMR}}$ ,  $\rho_{\text{insp}}$  and  $\rho_{\text{postinsp}}$  are the SNR of the full IMR signal, SNR upto a certain cutoff frequency, and SNR after the cutoff frequency respectively. In each case, the cutoff frequency is assumed to be the frequency at the innermost circular stable orbit (ISCO) corresponding to the remnant Kerr BH.

To avoid possible systematic biases in our parameter-estimation analysis due to error in waveform modeling, we use the GR version of the same waveform, SEOBNR (i.e., without allowing for deviations in the QNM parameters) to simulate our GW signal. And to avoid systematic biases due to noise, we use an averaged (zero-noise) realization of the

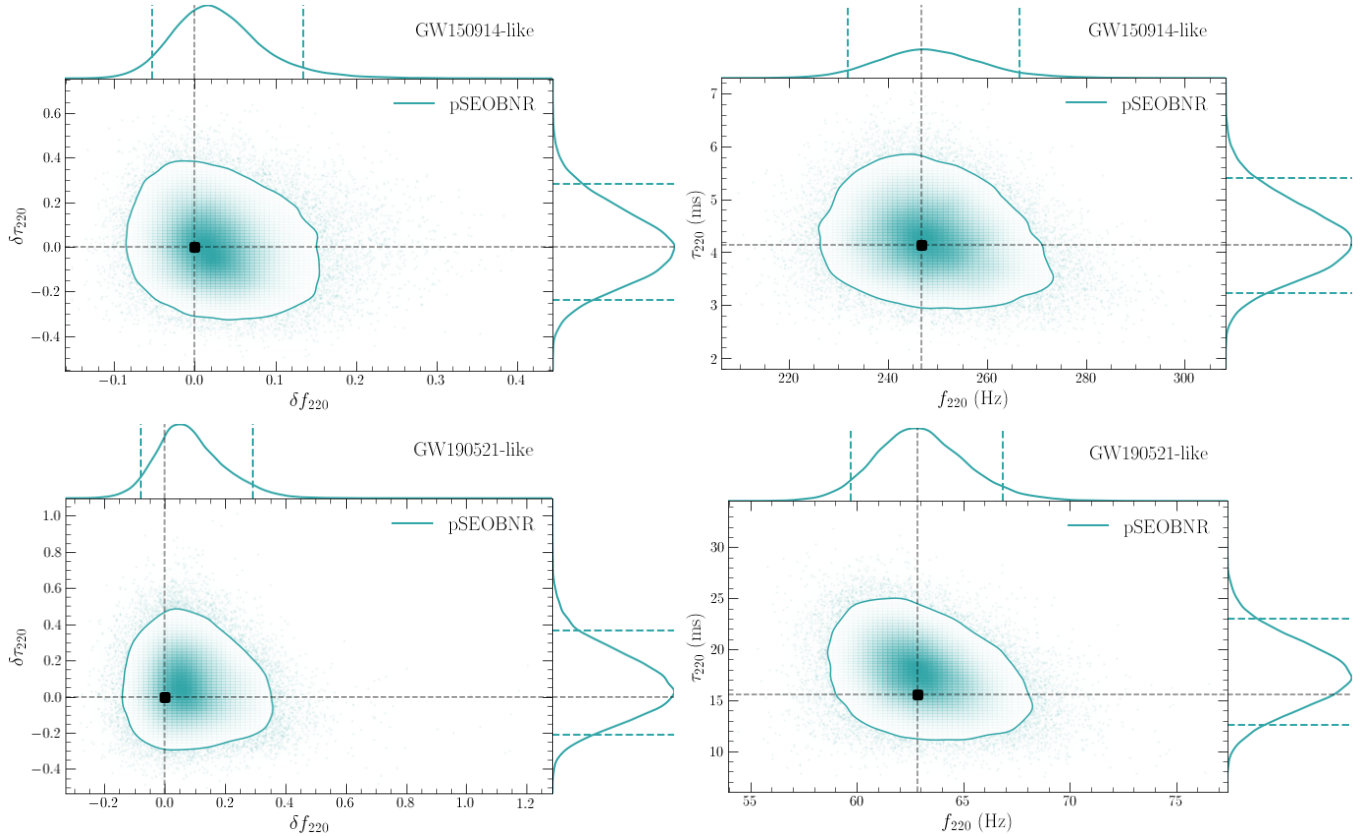


FIG. 1. Posterior probability distribution on the fractional deviations in the frequency and damping time of the (2, 2) QNM,  $(\delta f_{220}, \delta \tau_{220})$  (left panels) and the reconstructed quantities,  $(f_{220}, \tau_{220})$  (right panels) for GR injections (SEOBNR) with initial parameters similar to GW150914 (top panels) and GW190521 (bottom panels) (see Table I). The 2D contour marks the 90% credible region, while the dashed lines on the 1D marginalized distributions mark the 90% credible levels. The black vertical and horizontal lines mark the injection values.

noise<sup>1</sup>. Since nearly-equal-mass binaries like GW150914 and GW190521 observed at moderately high SNRs are not expected to have a loud ringdown signal, we restrict ourselves to estimating the frequency and damping time of only one QNM ( $\ell m$ ) = (2, 2) (i.e.,  $\{\delta f_{220}, \delta \tau_{220}\}$ ), while fixing the other QNM frequencies to their GR values.

We find, as one might expect, that the posterior distribution on the parameters describing fractional deviations in the frequency and damping time are consistent with zero (left panels of Fig. 1). One can then convert these fractional quantities into absolute quantities using the relations given in Eqs. (2.7a) and (2.7b), and construct posterior distributions on these effective quantities,  $(f_{220}, \tau_{220})$  (right panels of Fig. 1). In each of these cases, the recovered two-dimensional posteriors are consistent with the GR predictions (black dashed lines).

## B. Simulations using non-GR signals in Gaussian noise

To demonstrate the robustness of the method in detecting possible deviations from GR, we inject synthetic GW signals which are identical to the corresponding GR prediction up to merger, and differ in their post-merger description. We again choose binary-parameters similar to GW150914 and GW190521 (see Table I), but set  $\delta f_{220} = \delta \tau_{220} = 0.1$ . In other words, we assume that the frequency and damping time of our non-GR signal is 10% more than the corresponding GR prediction, although the pre-merger signal is identical to GR. In Fig. 2 we show this non-GR waveform, pSEOBNR with respect to the original GR template, SEOBNR. We see that the waveforms are identical in amplitude and instantaneous frequency upto the merger (lower panel), beyond which the red (GR template) and blue (non-GR template) differ. We summarize the results of the Bayesian analysis in Fig. 3 where we show the posterior probability distributions for  $(\delta f_{220}, \delta \tau_{220})$ , or equivalently  $(f_{220}, \tau_{220})$ . We find that they are consistent with the corresponding values of the injection parameters, indicated by the black dashed lines. We also note that at the SNRs we consider, since statistical uncertainties dominate systematic biases, the measurement excludes, at the 90% cred-

<sup>1</sup>A detailed study on noise systematics for one of the GW events is presented in Appendix A.

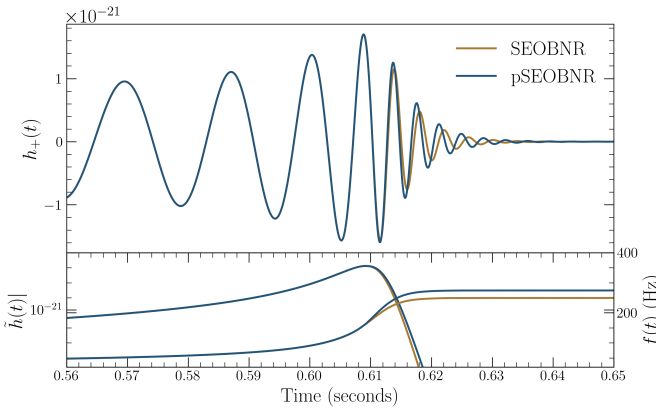


FIG. 2. Top panel: The ‘+’-polarization of the gravitational waveform  $h_+(t)$  from a GW150914-like event where the post-merger is described by GR (i.e.,  $\delta f_{220} = \delta\tau_{220} = 0$ ), and where the merger-ringdown is modified (i.e.,  $\delta f_{220} = \delta\tau_{220} = 0.1$ ). Bottom panel: Comparison of the evolution of the amplitude,  $|h(t)|$  (left) and instantaneous frequency,  $f(t)$  (right) for the GR and non-GR signal.

ible level, the GR prediction of the frequency ( $\delta f_{220} = 0$ ), but includes the prediction of the damping time ( $\delta\tau_{220} = 0$ ). However, with louder events, one would expect these measurement errors to shrink and the  $\tau_{220}$  measurement to be inconsistent with the GR prediction, as well.

We additionally investigate the effects of erroneously assuming that an underlying non-GR signal can be well-described by a GR one. We do this by estimating the parameters of our non-GR signals using the GR waveform model SEOBNR instead of the parameterized pSEOBNR. The resulting one- and two-dimensional posteriors are shown in the right panels of Fig. 3 by purple curves for the GW150914-like (top) and GW190521-like (bottom) signals respectively. For both signals, we find the 2D SEOBNR estimates are markedly biased with respect to the pSEOBNR estimates. We investigate this impact on the estimation of the GR parameters  $\xi_{\text{GR}}$  by changing the magnitude of deviation in the non-GR parameters more in Fig. 4. We restrict ourselves to a GW150914-like event, and for comparison, add a synthetic signal with  $\delta f_{220} = \delta\tau_{220} = 0.5$ , or 50 % deviation, alongside the 10% non-GR signal and a signal with no deviation (essentially GR) mentioned above. The left (right) panels show the posterior probability distributions of the three signals using the GR, SEOBNR (non-GR, pSEOBNR) waveform model. The first difference we note is the SEOBNR recoveries yield biased estimates when the underlying signal is non-GR, while the pSEOBNR recoveries do not. Furthermore, as we increase the deviations, while the SEOBNR recoveries expectedly get more biased, the pSEOBNR measurements are robust in consistently recovering the injected value. This gives us confidence that the pSEOBNR model can accurately measure QNM properties without biasing measurements of inspiral quantities, like masses and spins. To compute the samples of the final mass and spin in the last row, we start from the samples of the complex QNM frequencies ( $f_{220}, \tau_{220}$ ), which are obtained from the fractional deviation samples ( $\delta f_{220}, \delta\tau_{220}$ ) and

the GR-quantities ( $f_{220}^{\text{GR}}, \tau_{220}^{\text{GR}}$ ) using Eqs. (2.7a) and Eq. (2.7b), and then invert them using the fitting formula in Ref. [47]. The three BBH signals,  $\delta f_{220} = \delta\tau_{220} = 0, 0.1, 0.5$ , correspond to three unique sets of values for  $(M_f, \chi_f)$ . These predicted values are correctly recovered by the pSEOBNR waveform (bottom-right plot in Fig. 4), leading to three distinct and disjointed 2D posteriors on  $(M_f, \chi_f)$ , unlike the SEOBNR analysis (to reduce clutter in the plot, we just plot the injection values for  $\delta f_{220} = \delta\tau_{220} = 0$ .

### C. Test of the no-hair conjecture

Finally, we provide a simple demonstration of a test of the no-hair theorem using our model. As described in the introduction, any test of the no-hair theorem of BHs would need to involve independent measurements of (at least) two different QNMs.

Here, we use an NR GW signal from the SXS catalog [90] corresponding to a non-spinning BBH with mass-ratio  $q = 6$  (SXS:BBH:0166) and total mass  $M = 84M_\odot$  (see Table I). We choose an asymmetric system to increase the SNR in the higher modes. We also choose the distance and orientation of the binary such that the total SNR in the three-detector network of LIGO Hanford, Livingston and Virgo, is  $\sim 70$ . Based on the LIGO-Virgo observations during the first three observing runs, such asymmetric and loud signals are no longer just a theoretical prediction, but quite plausible during O4. Using this signal, we attempt to measure both the (2, 2) and (3, 3) QNMs. For this injected signal the SNR in other sub-dominant modes is too low to be able to measure them.

We summarize our results in Fig. 5. Given the injection parameters, the predicted values of the (2, 2) and (3, 3) frequency and damping time are (169.45 Hz, 4.68 ms) and (271.21 Hz, 4.50 ms) respectively. The left panel of Fig. 5 shows that the 2D posteriors on the (2, 2) and (3, 3) QNMs are consistent with the predictions for a BBH merger in GR, indicated by the black plus sign. Using fitting formulae provided in Ref. [47], specifically, Eq. (2.1), Eq. (E1) and Eq. (E3) and Tables VIII and IX for the fitting coefficients, we infer the 2D posterior probability distribution on the final mass and spin as predicted independently by the (2, 2) (blue) and (3, 3) (red) QNMs in the right panel of Fig. 5. The two independent estimates are consistent with each other and correspond to a unique mass and spin for the remnant BH ( $83.08 M_\odot, 0.37$ ) indicated by the plus sign. As a consequence, this may be considered as a test of the no-hair conjecture. For most of the events observed so far, the power in the (3, 3) has not been sufficient to measure it along with the (2, 2). However, it might also be possible to combine information from multiple observation over the coming few years to obtain meaningful constraints on the (3, 3) and other sub-dominant QNMs [53, 54, 91].

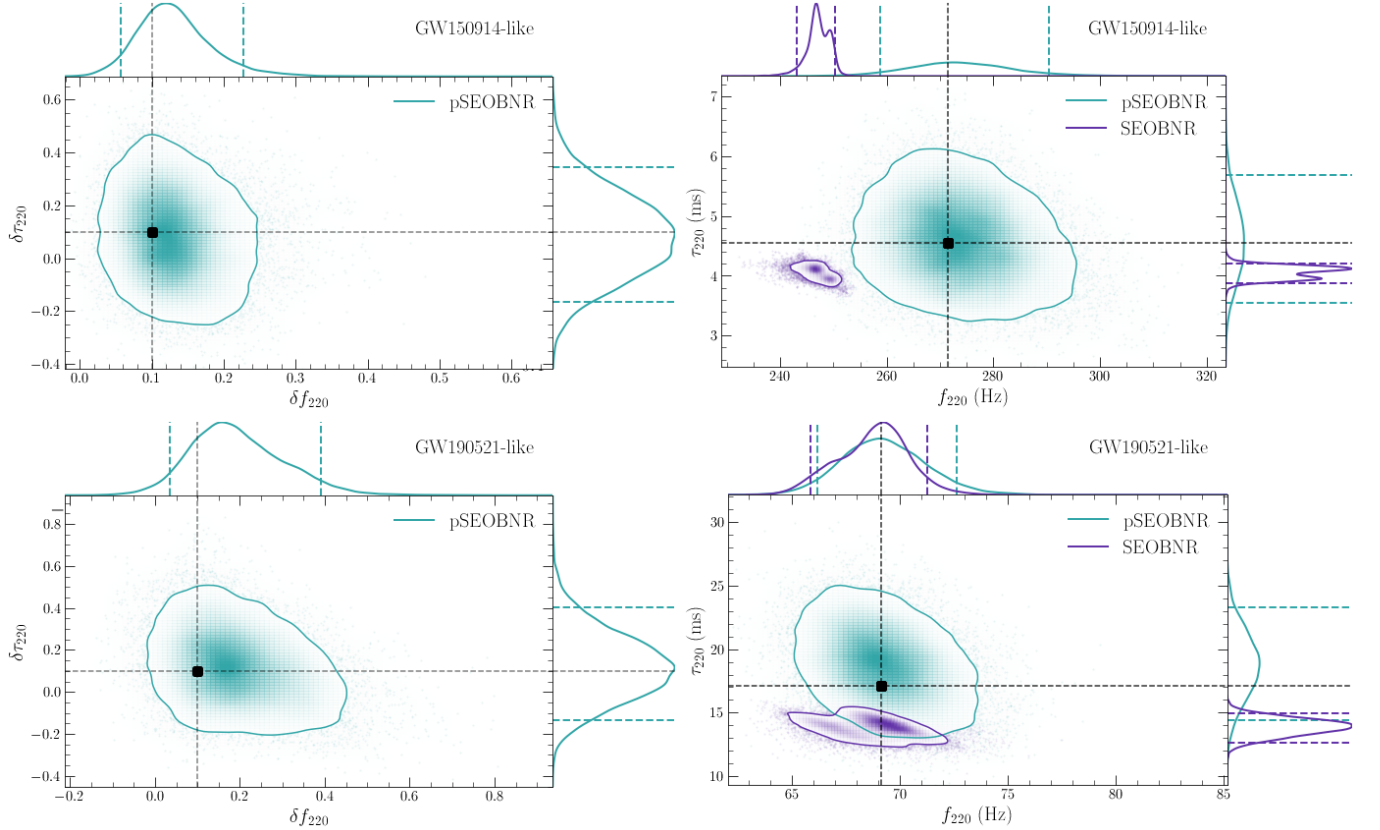


FIG. 3. Posterior probability distribution on the fractional deviations in the frequency and damping time of the (2, 2) QNM,  $(\delta f_{220}, \delta \tau_{220})$  (left panels) and the reconstructed quantities,  $(f_{220}, \tau_{220})$  (right panels) for non-GR injections (pSEOBNR) with parameters of GW150914-like (top panels) and GW190521-like (bottom panels) as given in Table I. The non-GR signal has a deviation,  $\delta f_{220} = \delta \tau_{220} = 0.1$ . The 2D contour marks the 90% credible region, while the dashed lines on the 1D marginalized distributions mark the 90% credible levels. The black vertical and horizontal lines mark the injection values. In the right panels, we additionally show measurements using a GR (SEOBNR) waveform, for the GW150914-like (upper panel) and GW190521-like (lower panel) injections. The measurements with SEOBNR waveforms are visibly biased.

#### IV. CONSTRAINTS ON QNM FREQUENCIES USING LIGO-VIRGO DATA

The LIGO-Virgo Collaboration recently released their testing GR catalogue containing results for events observed during O3a [19]. For the test that we here present, the results shown in Ref. [19] only include events which pass a threshold for the median detector-frame total mass  $\geq 90M_\odot$  and SNRs in the pre- and post-merger regions  $\geq 8$ <sup>1</sup>. The SNR threshold ensures that the signal contains sufficient information in both the inspiral and merger stages to break the degeneracy between the binary's total mass and the non-GR deviations  $(\delta f_{220}, \delta \tau_{220})$ . Such strong degeneracy is present for low-SNR events with negligible higher-modes and for which

only the post-merger is detectable rendering the measurement of  $(\delta f_{220}, \delta \tau_{220})$  impossible for those cases (see Appendix B for more details). On the other hand the total mass threshold  $\geq 90M_\odot$  was employed due to the fact that this analysis is computationally expensive, and also because we expected these events to be the most promising for ringdown studies. However, since the SNR threshold alone should be sufficient for the analysis, for this paper we run the test on all the events listed in Ref. [19] that have SNRs in the pre- and post-merger regions  $\geq 8$ , without imposing any mass threshold.

Given the above we add the signals GW190630\_185205 and GW190828\_063405, to the list of GW events considered in Ref. [19]. Furthermore, for the first time, we apply our method to measure the QNMs to GW events from O1 and O2, notably GW150914 and GW170104. The other high-mass events from O1 and O2, GW170729, GW170809, GW170814, GW170818 and GW170823 do not have an SNR  $\geq 8$  in the merger-ringdown signal. The list of the signals for which we run the analysis is given in Table II.

For all the relevant signals, we show the posterior distributions  $(\delta f_{220}, \delta \tau_{220})$  in the left panel of Fig. 6 and also provide

<sup>1</sup>The pre- and post-merger regions of the signal are identified from the signal's power before and after the signal reaches the peak's amplitude, which is determined from the maximum of the likelihood function obtained with the parameter-estimation analysis. The SNR values are listed in Table IV of Ref. [19]

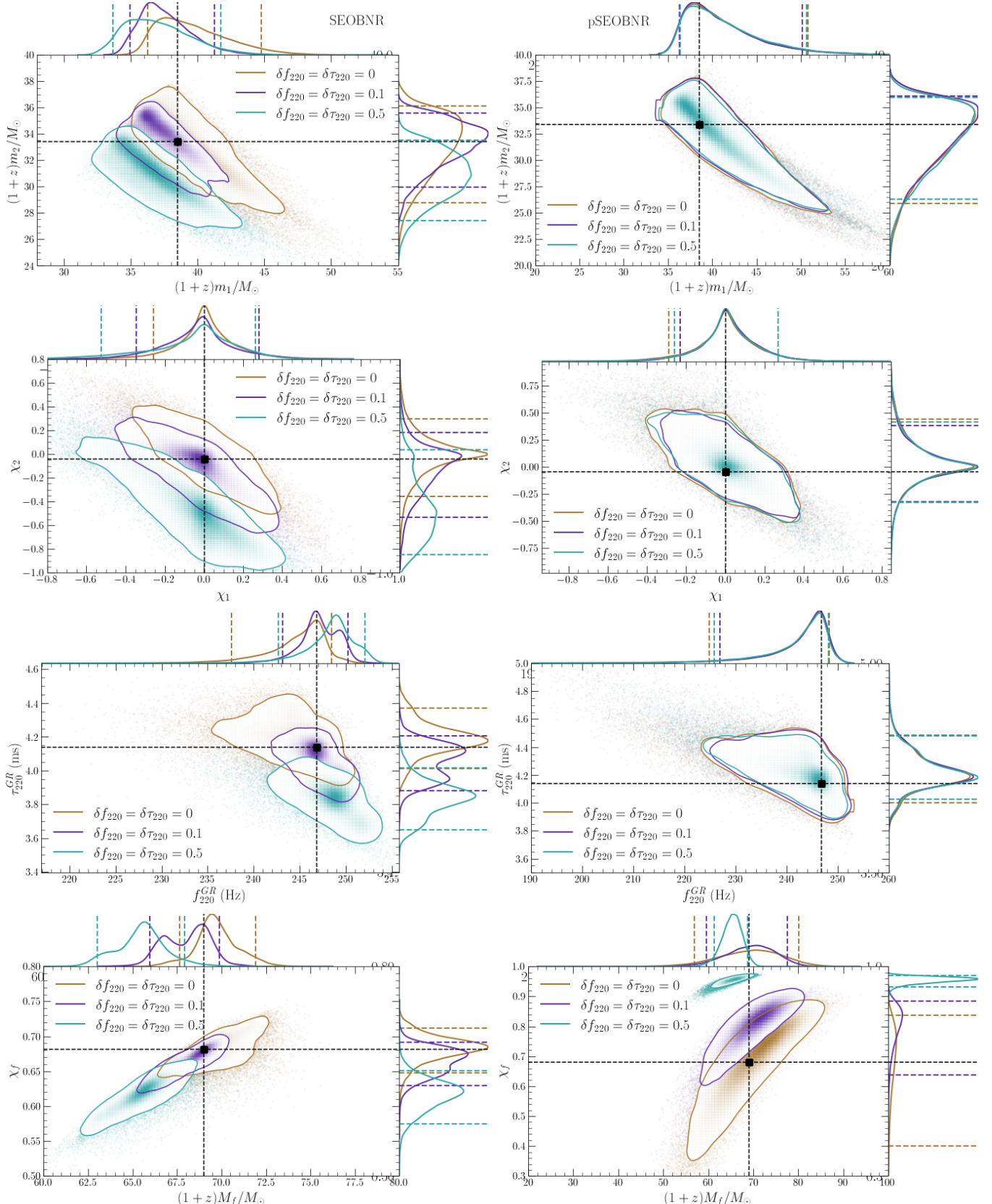


FIG. 4. Comparison of a GW150914-like injection's parameters when signals with zero, 10% and 50% deviations ( $\delta f_{220} = \delta \tau_{220} = 0, 0.1, 0.5$ ) are recovered using a GR (SEOBNR) (left panels) or a non-GR (pSEOBNR) (right panels) waveform model. The panels (from top to bottom) show the 2D posteriors (with 90% credible levels) and corresponding marginalised 1D posteriors (with 90% credible levels) in (detector-frame) masses (first row), dimensionless spins (second row), GR predictions of frequency and damping time (third row) and the remnant mass and spin predictions ( $M_f, \chi_f$ ) (fourth row) from the frequency and damping time. In each case, the injection values are indicated by the black dashed lines. In the lowermost panel, the injection values of the final mass and spin, correspond to the injection with no deviations. The  $\delta f_{220} = \delta \tau_{220} = 0.1$  signal is identical to the results shown in Fig. 3.

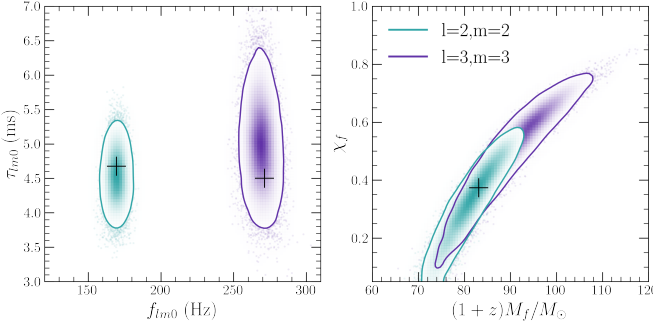


FIG. 5. Posterior probability distribution on the frequency and damping time of the (2, 2) and (3, 3) QNM (left panel), and the final mass and spin inferred from the complex frequencies (right panel), when a NR signal with parameters  $q = 6$ ,  $M = 84M_\odot$  and  $\text{SNR} = 75$  is injected in Gaussian noise and recovered with the pSEOBNR waveform model. The plus signs mark the GR predictions.

the reconstructed QNM parameters,  $(f_{220}, \tau_{220})$  in Table II. In the right panel of Fig. 6 we also provide a summary of the 90% credible intervals on the 1D marginalized posteriors. We highlight the dependence of the constraints on the total mass of the system. In general, the tightest bounds are set by the most massive systems, as they tend to have larger post-merger SNR. We find a similar trend in the right panel of Fig. 6.

Among all the GW signals detected so far, GW150914 (solid curve in Fig. 6) is unique in its loudness, leading to the first, and to date, best attempt in measuring the QNM frequencies [16, 48–50]. Within 90% credibility we obtain from GW150914:

$$\delta f_{220} = 0.05^{+0.11}_{-0.07} \quad \delta \tau_{220} = 0.07^{+0.26}_{-0.23}. \quad (4.1)$$

Stronger constraints can be obtained by combining information from all the events [19]. If we assume that the fractional deviations  $(\delta f_{220}, \delta \tau_{220})$  take the same values in multiple events, we can assume the posterior of one event to be the prior for the next, and obtain a joint posterior probability distribution. For  $N$  observations, where  $P(\delta f_{220}, \delta \tau_{220}|d_j)$  is the posterior for the  $j$ -th observation corresponding to the data set  $d_j$ ,  $j = 1, \dots, N$ , the joint posterior is given by:

$$P(\delta f_{220}, \delta \tau_{220}| \{d_j\}) = P(\delta f_{220}, \delta \tau_{220}) \prod_{j=1}^N \frac{P(\delta f_{220}, \delta \tau_{220}|d_j)}{P(\delta f_{220}, \delta \tau_{220})}, \quad (4.2)$$

where  $P(\delta f_{220}, \delta \tau_{220})$  is the prior on  $(\delta f_{220}, \delta \tau_{220})$ . However, since here we assume the prior on  $(\delta f_{220}, \delta \tau_{220})$  to be flat (or uniform), the joint posterior is equal to the joint likelihood. We show these joint likelihoods on  $(\delta f_{220}, \delta \tau_{220})$ , as well as, the corresponding 1D marginalized distributions as filled grey curves in Fig. 6. From the joint likelihood we obtain within 90% credibility:

$$\delta f_{220} = 0.02^{+0.04}_{-0.04}, \quad \delta \tau_{220} = 0.10^{+0.14}_{-0.14}. \quad (4.3)$$

However, in most non-GR theories, the deviations parameters  $(\delta f_{220}, \delta \tau_{220})$  depend in general on the source's parameters, so if GR were to be wrong, one should expect their value

to vary across the GW signals observed by LIGO and Virgo. As described in Ref. [19], we can relax the assumption of a constant deviation across all events by using the hierarchical inference technique originally proposed in Refs. [92, 93]. The general idea behind this technique is to assume that the non-GR parameters  $(\delta f_{220}, \delta \tau_{220})$  are drawn from a common underlying distribution, whose properties can be inferred from the population of events. Following [19, 92, 93] we model the population distribution with a Gaussian  $\mathcal{N}(\mu, \sigma)$  of unknown mean  $\mu$  and standard deviation  $\sigma$ . Under those assumptions, the goal is then to directly measure a posterior distribution  $P(\mu, \sigma| \{d_j\})$  for  $\mu$  and  $\sigma$  from a joint analysis of all the GW events. If GR is correct, then this posterior should be consistent with  $\mu = 0$  and  $\sigma = 0$ . From Bayes' theorem it follows that [93]:

$$P(\mu, \sigma| \{d_j\}) \propto P(\mu, \sigma) \prod_{j=1}^N P(d_j|\mu, \sigma), \quad (4.4)$$

where  $P(\mu, \sigma)$  is the prior (also known as hyperprior) on  $(\mu, \sigma)$ , and  $P(d_j|\mu, \sigma)$  can be written in terms of the individual likelihoods of a given non-GR parameter  $\xi_{\text{nGR}}$  using [93]

$$P(d_j|\mu, \sigma) = \int P(d_j|\xi_{\text{nGR}}) P(\xi_{\text{nGR}}|\mu, \sigma) d\xi_{\text{nGR}}. \quad (4.5)$$

Here  $P(\xi_{\text{nGR}}|\mu, \sigma) = \mathcal{N}(\mu, \sigma)$  by construction and  $P(d_j|\xi_{\text{nGR}})$  is the likelihood for the parameter  $\xi_{\text{nGR}}$  for a given event  $d_j$  that is computed from the standard parameter estimation analysis. After obtaining  $P(\mu, \sigma| \{d_j\})$ , we can then infer a population distribution for a given non-GR parameter  $\xi_{\text{nGR}}$  using [93]:

$$P(\xi_{\text{nGR}}| \{d_j\}) = \int P(\xi_{\text{nGR}}|\mu, \sigma) P(\mu, \sigma| \{d_j\}) d\mu d\sigma. \quad (4.6)$$

Notice that, if we fix  $\sigma = 0$ , this approach is equivalent to assume that all events share the same non-GR parameter  $\xi_{\text{nGR}} = \mu$  and Eq. (4.6) reduces to the joint likelihood [92]. In practice, we use the stan-based code [94] developed and used in Refs. [19, 93] to obtain  $P(\mu, \sigma| \{d_j\})$  and compute  $P(\xi_{\text{nGR}}| \{d_j\})$ .

The 1D posteriors for  $\delta f_{220}$  and  $\delta \tau_{220}$  obtained with this technique are shown in Fig. 6 (dash-dotted curves) with corresponding median and 90% credible interval given by:

$$\delta f_{220} = 0.03^{+0.10}_{-0.09}, \quad \delta \tau_{220} = 0.10^{+0.44}_{-0.39}. \quad (4.7)$$

Compared to Ref. [19] these constraints are almost a factor  $\sim 4$  more stringent for  $\delta f_{220}$  and a factor  $\sim 2$  for  $\delta \tau_{220}$ . Similar improvements hold for the hyperparameters:  $\delta f_{220}$  ( $\mu = 0.03^{+0.06}_{-0.05}$ ,  $\sigma < 0.09$ ) and  $\delta \tau_{220}$  ( $\mu = 0.11^{+0.21}_{-0.19}$ ,  $\sigma < 0.39$ ).

## V. DISCUSSION

We have built a parameterized IMR waveform model, pSEOBNR, that can measure the QNM complex frequencies of the remnant object formed through the merger of BHs

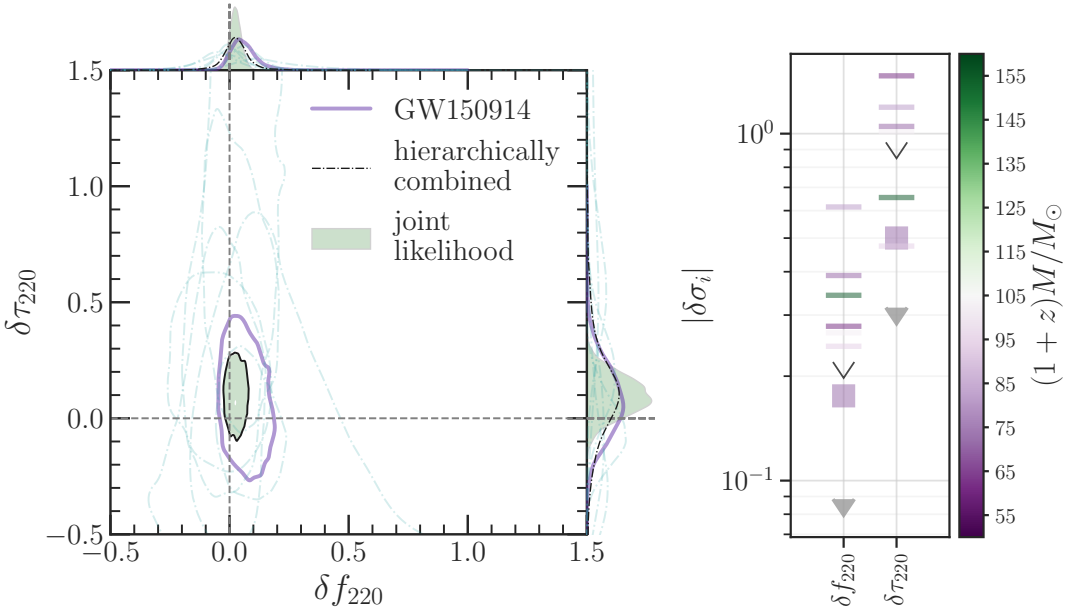


FIG. 6. *Left panel:* The 90% credible levels of the posterior probability distribution of the fractional deviations in the frequency and damping time of the (2, 2) QNM,  $(\delta f_{220}, \delta \tau_{220})$  and their corresponding one-dimensional marginalized posterior distributions, for events from O1, O2 and O3a passing a SNR threshold of 8 in both the pre- and post-merger signal. The solid purple curve marks the best single-event constraint, GW150914, whereas the constraints from the other events are indicated by the dash-dot curves. The joint constraints on  $(\delta f_{220}, \delta \tau_{220})$  obtained multiplying the likelihoods from individual events is given by the filled grey contours, while the hierarchical method of combination yields the black dot dashed curves. *Right panel:* 90% credible interval on the one-dimensional marginalised posteriors on  $\delta \sigma_i = (\delta f_{220}, \delta \tau_{220})$ , colored by the median redshifted total mass  $(1+z)M$ , inferred assuming GR. Filled gray (unfilled black) triangles mark the constraints obtained when all the events are combined by multiplying likelihoods (hierarchically). The purple square marker indicates constraints from the single most-prominent event, GW150914.

| Event           | $f_{220}$ (Hz)           | $\tau_{220}$ (ms)       | $(1+z)M_f/M_\odot$      | $\chi_f$               | $(1+z)M_f^{\text{IMR}}/M_\odot$ | $\chi_f^{\text{IMR}}$  |
|-----------------|--------------------------|-------------------------|-------------------------|------------------------|---------------------------------|------------------------|
| GW150914        | $257.6^{+17.0}_{-12.8}$  | $4.49^{+1.09}_{-0.95}$  | $71.0^{+8.7}_{-10.3}$   | $0.77^{+0.09}_{-0.18}$ | $67.3^{+2.7}_{-2.6}$            | $0.67^{+0.03}_{-0.04}$ |
| GW170104        | $291.4^{+14.7}_{-30.1}$  | $5.53^{+3.47}_{-2.40}$  | $73.8^{+11.1}_{-19.8}$  | $0.89^{+0.07}_{-0.36}$ | $56.9^{+3.0}_{-3.0}$            | $0.65^{+0.05}_{-0.07}$ |
| GW190519_153544 | $123.6^{+11.9}_{-13.0}$  | $10.33^{+3.56}_{-3.07}$ | $155.5^{+24.0}_{-29.9}$ | $0.81^{+0.10}_{-0.28}$ | $144.1^{+14.5}_{-16.2}$         | $0.78^{+0.08}_{-0.14}$ |
| GW190521_074359 | $204.6^{+14.6}_{-11.7}$  | $5.32^{+1.48}_{-1.21}$  | $86.4^{+12.2}_{-14.3}$  | $0.73^{+0.12}_{-0.26}$ | $87.1^{+3.3}_{-3.8}$            | $0.70^{+0.03}_{-0.05}$ |
| GW190630_185205 | $247.8^{+31.8}_{-52.8}$  | $3.87^{+2.37}_{-1.80}$  | $65.6^{+18.8}_{-41.5}$  | $0.62^{+0.27}_{-0.62}$ | $66.2^{+4.0}_{-3.2}$            | $0.70^{+0.05}_{-0.08}$ |
| GW190828_063405 | $257.8^{+201.3}_{-27.8}$ | $4.23^{+4.17}_{-1.92}$  | $67.4^{+25.7}_{-30.0}$  | $0.76^{+0.20}_{-0.73}$ | $75.8^{+5.0}_{-5.0}$            | $0.74^{+0.04}_{-0.06}$ |
| GW190910_112807 | $174.2^{+11.7}_{-7.5}$   | $9.52^{+3.13}_{-2.68}$  | $123.5^{+14.7}_{-18.1}$ | $0.90^{+0.05}_{-0.11}$ | $94.9^{+7.6}_{-8.6}$            | $0.72^{+0.08}_{-0.04}$ |

TABLE II. The median and symmetric 90% credible intervals of the remnant properties. The first two columns represent the frequency and damping time of the (2, 2) QNM measured using the pSEOBNR model. The next two columns are the mass and spin of the remnant object estimated from the complex QNM frequencies by inverting the fitting formula in [47]. The last two columns represent final mass and spin estimates predicted using NR fitting formulae from a SEOBNR parameter estimation.

with aligned or antialigned spins, thus extending previous work, which was limited to non-spinning BHs [48]. The pSEOBNR model was recently used to infer the QNMs of some of the BBH's remnants detected by LIGO and Virgo during O3a [19].

After testing our method to infer the QNM frequencies with GR and non-GR synthetic-signal injections in Gaussian noise, we have applied it to LIGO and Virgo real data. We have analyzed GW events in O1, O2 and O3a (a total of 4 new events) that were not examined in Ref. [19] with the pSEOBNR model (see Table II). After combining our new results with the other GW events in O3a investigated with our method [19],

we have obtained more stringent bounds on the dominant (or least-damped) QNM to date ( $\ell = 2, m = 2$ ).

More specifically, as expected, the single GW event providing the best constraint on the least-damped QNM to date continues to be GW150914 ( $\delta f_{220} = 0.05^{+0.11}_{-0.07}$ ,  $\delta \tau_{220} = 0.07^{+0.26}_{-0.23}$ ), although the bounds on  $\delta \tau_{220}$  from GW150914 are comparable to GW190521\_074359, the second-most precisely measured event in our list. In addition, in the most agnostic and conservative scenario where we combine the information from different events using a hierarchical approach [92, 93], we obtain at 90% credibility ( $\delta f_{220} = 0.03^{+0.10}_{-0.09}$ ,  $\delta \tau_{220} = 0.10^{+0.44}_{-0.39}$ ). Thus, our results constrain the frequency (decay time) of the

least damped QNM to be within  $\sim 10\%$  ( $\sim 40\%$ ) of the GR prediction — an improvement of a factor of  $\sim 4$  ( $\sim 2$ ) over the results obtained with the pSEOBNR model in Ref. [19].

Furthermore, when assuming that the deviations from GR do not vary appreciably over the GW events that we have analyzed, and combine the likelihood functions, we have obtained the most stringent bounds on the dominant QNM ( $\delta f_{220} = 0.02^{+0.04}_{-0.04}, \delta \tau_{220} = 0.10^{+0.14}_{-0.14}$ ). Those constraints are compatible, but slightly better (especially for the decay time) than the ones recently reported in Ref. [95] (see first row in Table II therein), where QNM frequencies were inferred using only the post-merger part of the signal. We note that Ref. [95] used a larger set of GW events from O1, O2 and O3a than we did, although we expect that the extra GW events will not contribute significantly to the combined bound since they have lower SNRs.

These constraints could in principle be used to constrain specific non-GR theories and exotic compact objects [96–98]. However, QNM computations in non-GR theories have only been done in a handful of cases, mostly focusing on non-rotating or slowly-rotating BH solutions [99–116], or relying on the eikonal/geometric optics approximation to obtain estimates of the QNMs for spinning BHs [102, 117, 118]. The only exceptions to this rule, that we are aware of, are computations of the QNM of Kerr-Newman BHs in Einstein-Maxwell theory [119–122] or estimates of the BBH in non-GR theories obtained through a limited number of NR simulations [123, 124]. Given these limitations, our ability of going beyond a null test of GR and use our results to impose precise constraints on non-GR theories with QNM measurements is currently quite limited.

Despite these theoretical limitations there has been some recent effort to develop parametrizations that could help mapping measurements of the parameters ( $\delta f_{\ell m 0}, \delta \tau_{\ell m 0}$ ) onto constraints to specific non-GR theories. This includes for example the parametrization proposed in Ref. [59], recently applied to LIGO-Virgo GW events in Ref. [95], where deviations from the GR QNMs explicitly depend on a perturbative expansion in the BH spin and possible extra non-GR parameters, or the proposal of Refs. [125, 126] where deviations from the GR QNMs are mapped onto generic small modifications of the perturbation equations describing the QNMs. Other examples also include proposals to map deviations from the GR QNMs to coefficients in generic effective-field-theory actions [105, 106, 114] or to directly relate measurements of the QNM complex frequencies to a parametrized non-GR BH metric [117, 127, 128], which could be then used jointly with measurements from the Event Horizon Telescope to obtain stronger constraints on deviations from GR [128–131]. We should note, however, that all these parametrizations are either limited to non-spinning BHs or make use of a series expansion in the BH spin which might limit their accuracy for highly-spinning BHs, unless the sensitivity of GW detectors will not allow us to access the higher coefficients in the spin series.

In the future, it would be important to test whether the pSEOBNR model could be used to detect deviations in waveforms obtained through NR simulations of specific non-GR

theories. Such results are still at their infancy and have so far only been done for a handful of theories, focusing mostly on proof-of-concept simulations [123, 124, 132–139]. Nonetheless, given the recent efforts put forward in order to simulate BBHs in non-GR theories, we hope that accurate non-GR IMR waveforms will become available in the near future.

Finally, an obvious generalization of this work would be to extend the parameterized pSEOBNR model to generic precessing BBHs, which can in principle be easily done using the recently developed multipolar EOB model reported in Ref. [140]. Lastly, it will be relevant to include GR deviations in the pSEOBNR model also during the late inspiral and plunge stages of the BBH coalescence. On the other hand, GR deviations (notably deviations from PN theory) for the long inspiral stage are currently available in the pSEOBNR model and have been used to set bounds on the PN parameters in the GW phasing using LIGO and Virgo observations [17–19].

## ACKNOWLEDGEMENTS

The authors thank Max Isi for generously allowing us to use the code developed in Ref. [93] for the hierarchical inference analysis, and Gregorio Carullo for carefully reading the manuscript and providing useful comments. The authors would like to thank everyone at the frontline of the Covid-19 pandemic. The authors are grateful for computational resources provided by the LIGO Laboratory and supported by the National Science Foundation Grants PHY-0757058 and PHY-0823459, as well as computational resources at the AEI, specifically the Hypatia cluster. R.B. acknowledges financial support from the European Union’s Horizon 2020 research and innovation programme under the Marie Skłodowska-Curie grant agreement No. 792862, from the European Union’s H2020 ERC, Starting Grant agreement no. DarkGRA-757480, and from the MIUR PRIN and FARE programmes (GW-NEXT, CUP: B84I20000100001). We also acknowledge support from the Amaldi Research Center funded by the MIUR program “Dipartimento di Eccellenza” (CUP: B81I18001170001).

## Appendix A: Study of systematics in ringdown measurements in real, non-Gaussian noise

Inferences of all parameters in this paper have been done under the assumption that the noise in the detectors is stationary and Gaussian. In other words, detector noise follows a normal distribution with zero mean and a PSD,  $S_n(f)$ , that is not a function of time, at least during the duration of the GW signal. This allows us to write the Bayesian likelihood function in the form given in Eqs. (2.10) and (2.11), and perform all the parameter estimation that follows in the results sections. However, LIGO-Virgo noise can often have features that deviate from stationarity and Gaussianity. If such features are not taken into account appropriately, final estimates of parameters can get biased. Here we demonstrate one such case by injecting in real noise a GW190521-like signal and

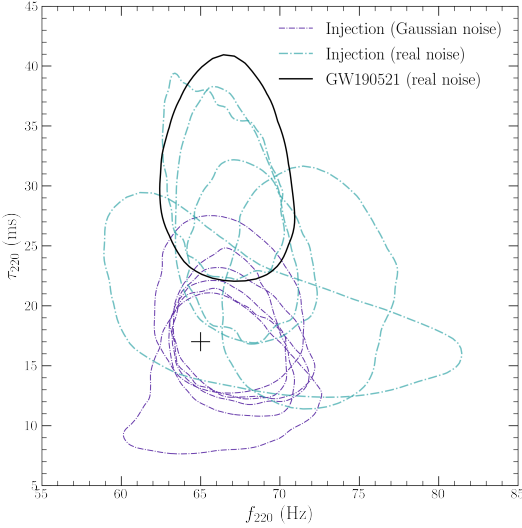


FIG. 7. 90 % credible level on the posterior probability distribution of the frequency and damping time of (2, 2) mode,  $(f_{220}^{\text{GR}}, \tau_{220}^{\text{GR}})$  using synthetic NRSur signals with parameters similar to the GW event, GW190521, in Gaussian noise (grey dot-dashed lines) and real interferometric noise (green dot dashed lines). The GR prediction for the frequency and damping time is indicated by the black cross. While the Gaussian noise simulations are consistent with the prediction, at least 3 of the 5 real noise simulation are not. The black curve corresponds to the measurements of the real event GW190521 reported in Ref. [19]. All signals are recovered using the pSEOBNR model.

showing how parameter estimates can be biased when our description of detector noise is not complete.

We choose a spinning, precessing NR-surrogate model NRSur<sup>1</sup> (valid up to mass ratio 4) to simulate the actual GW190521 signal observed by the LIGO and Virgo detectors [39] (see Table I of Ref. [39])). The choice of the NRSur model is motivated by the fact that it is the most accurate model in the parameter range described by GW190521, because it is built by directly interpolating NR waveforms. In Fig. 7, we indicate with a black cross what the injected NRSur signal predicts for the QNM ( $\ell = 2, m = 2$ ) frequency and damping time. For comparison, we also show with a black solid curve the results obtained when recovering the actual signal GW190521 with the pSEOBNR model. As seen in the plot, while the measurement of the frequency is consistent with the prediction, we overestimate the damping time.

To understand such offset in the decay time, we proceed as follows. The actual GW190521 event was observed at a GPS time, 1242442967.61 seconds (roughly 03:02:49 UTC, May 21, 2019). We select a time period of about 2.5 hours around this GPS time, create synthetic signals with the NRSur model and inject them in different stretches of the real detector noise around the time of the actual GW event. The PSDs of GW detectors are expected to vary over longer durations of time,

and hence the 2.5 hour stretch of noise we consider can be assumed to have noise-properties similar to the time of the actual event. Then, we perform Bayesian analysis against those injections using the pSEOBNR model. The results are indicated by green curves in Fig. 7. As it can be seen from the figure, for 3 of the 5 noise realizations, corresponding to  $t_0 - 1$  hour,  $t_0 + 0.5$  hours, and  $t_0 + 1$  hour, we recover a damping time similar to the one obtained when using the pSEOBNR model against the actual event GW190521 (black curve), where  $t_0$  is the GPS time of the actual event. For the other two noise realizations, the pSEOBNR model estimates consistently the damping time, but has an off-set frequency, while the fifth noise realization is consistent with both predictions. This study suggests that a bias in the measurements of the damping time for the actual event GW190521 can be explained as due to an incomplete description of the noise at the time of the event.

The reader might question the judiciousness of using an aligned-spin waveform model, like pSEOBNR, to measure a signal like GW190521 which appears to be precessing, especially because an incomplete understanding of the underlying signal can also lead to biases in measured quantities, as we have already demonstrated in Sec. III B. In order to explore possible effects of missing information about in-plane spins in the pSEOBNR model, we repeat the above study of injecting synthetic signals using NRSur and recovering using the pSEOBNR model, but this time, instead of using real detector noise, we use Gaussian noise (i.e., realizations of noise sampled from a predicted detector PSD). Since the properties of the noise are completely understood in this case, any residual measurement biases can be completely attributed to differences in the waveform model. The 2D posterior distributions of the frequency and damping time measured using these Gaussian-noise signals are shown by the grey curves in Fig. 7. We find the measurements to be completely consistent with the predictions of the frequency and damping time, thus concluding that a lack of in-plane spins in the pSEOBNR model does not affect our measurements of the QNM properties. The fact that the measurement of ringdown quantities are robust against an incomplete description of the inspiral signal is a crucial property of our method.

## Appendix B: Correlation of the binary's total mass with the non-GR parameters

As mentioned in the main text, for low-SNR events with negligible higher-modes and for which only the post-merger is detectable, there is a strong degeneracy between the binary's total mass and the non-GR deviations ( $\delta f_{220}, \delta \tau_{220}$ ). For those cases, only the reconstructed frequency and damping time ( $f_{220}, \tau_{220}$ ) can be independently measured from the data. To justify this statement, in Fig. 8 we show corner plots that illustrate the correlations between the non-GR parameters ( $\delta f_{220}, \delta \tau_{220}$ ), the detector-frame total mass  $M(1+z)$  and the reconstructed frequency and damping time ( $f_{220}, \tau_{220}$ ) for GW150914 (left panel), corresponding to an event for which both the pre- and post-merger phase are measurable, and for GW190521 (right panel), an event in which the post-merger

<sup>1</sup>This waveform model is called NRSur7dq4 in LAL.

has SNR > 8, but the pre-merger has an SNR below 8. For GW190521, due the strong degeneracy between  $\delta f_{220}$  and  $M(1+z)$ , the 1D posterior for  $M(1+z)$  is pushed towards the upper boundary of its prior, despite the very wide prior employed in the analysis. This in turn renders the measurement of  $\delta f_{220}$  (and to a lesser degree of  $\delta\tau_{220}$ ) highly dependent on the upper boundary of the total mass prior. On the

other hand, this issue does not significantly affect the posteriors for the reconstructed quantities ( $f_{220}, \tau_{220}$ ) which are well measured and nearly independent on the upper prior boundary for  $M(1+z)$ . This is to be contrasted with the results for GW150914. In this case, the extra information coming from the pre-merger phase allows to break the degeneracy between the non-GR parameters and the total mass, and therefore both ( $\delta f_{220}, \delta\tau_{220}$ ) and  $M(1+z)$  can be measured at the same time.

- 
- [1] *LIGO scientific collaboration*, <https://www.ligo.org/>.
  - [2] *Virgo collaboration*, <https://www.virgo-gw.eu/>.
  - [3] R. Abbott et al. (LIGO Scientific, Virgo) (2020), 2010.14527.
  - [4] B. P. Abbott et al. (LIGO Scientific, Virgo), Phys. Rev. X **9**, 031040 (2019), 1811.12907.
  - [5] J. Aasi et al. (LIGO Scientific), Class. Quant. Grav. **32**, 074001 (2015), 1411.4547.
  - [6] F. Acernese et al. (VIRGO), Class. Quant. Grav. **32**, 024001 (2015), 1408.3978.
  - [7] A. H. Nitz, C. Capano, A. B. Nielsen, S. Reyes, R. White, D. A. Brown, and B. Krishnan, Astrophys. J. **872**, 195 (2019), 1811.01921.
  - [8] A. H. Nitz, T. Dent, G. S. Davies, S. Kumar, C. D. Capano, I. Harry, S. Mozzon, L. Nuttall, A. Lundgren, and M. Tápai, Astrophys. J. **891**, 123 (2019), 1910.05331.
  - [9] T. Venumadhav, B. Zackay, J. Roulet, L. Dai, and M. Zaldarriaga, Phys. Rev. D **101**, 083030 (2020), 1904.07214.
  - [10] B. Zackay, L. Dai, T. Venumadhav, J. Roulet, and M. Zaldarriaga (2019), 1910.09528.
  - [11] B. P. Abbott et al. (LIGO Scientific, Virgo), Phys. Rev. Lett. **116**, 061102 (2016), 1602.03837.
  - [12] B. P. Abbott et al. (LIGO Scientific, Virgo), Astrophys. J. Lett. **818**, L22 (2016), 1602.03846.
  - [13] B. P. Abbott et al. (LIGO Scientific, Virgo, Fermi GBM, INTEGRAL, IceCube, AstroSat Cadmium Zinc Telluride Imager Team, IPN, Insight-Hxmt, ANTARES, Swift, AGILE Team, 1M2H Team, Dark Energy Camera GW-EM, DES, DLT40, GRAWITA, Fermi-LAT, ATCA, ASKAP, Las Cumbres Observatory Group, OzGrav, DWF (Deeper Wider Faster Program), AST3, CAASTRO, VINROUGE, MASTER, J-GEM, GROWTH, JAGWAR, CaltechNRAO, TTU-NRAO, NuSTAR, Pan-STARRS, MAXI Team, TZAC Consortium, KU, Nordic Optical Telescope, ePESSTO, GROND, Texas Tech University, SALT Group, TOROS, BOOTES, MWA, CALET, IKI-GW Follow-up, H.E.S.S., LOFAR, LWA, HAWC, Pierre Auger, ALMA, Euro VLBI Team, Pi of Sky, Chandra Team at McGill University, DFN, ATLAS Telescopes, High Time Resolution Universe Survey, RIMAS, RATIR, SKA South Africa/MeerKAT), Astrophys. J. Lett. **848**, L12 (2017), 1710.05833.
  - [14] B. P. Abbott et al. (LIGO Scientific, Virgo, Fermi-GBM, INTEGRAL), Astrophys. J. Lett. **848**, L13 (2017), 1710.05834.
  - [15] B. P. Abbott et al. (LIGO Scientific, Virgo, 1M2H, Dark Energy Camera GW-E, DES, DLT40, Las Cumbres Observatory, VINROUGE, MASTER), Nature **551**, 85 (2017), 1710.05835.
  - [16] B. P. Abbott et al. (LIGO Scientific, Virgo), Phys. Rev. Lett. **116**, 221101 (2016), [Erratum: Phys.Rev.Lett. 121, 129902 (2018)], 1602.03841.
  - [17] B. P. Abbott et al. (LIGO Scientific, Virgo), Phys. Rev. Lett. **123**, 011102 (2019), 1811.00364.
  - [18] B. P. Abbott et al. (LIGO Scientific, Virgo), Phys. Rev. D **100**, 104036 (2019), 1903.04467.
  - [19] R. Abbott et al. (LIGO Scientific, Virgo) (2020), 2010.14529.
  - [20] L. Blanchet, Living Rev. Rel. **17**, 2 (2014), 1310.1528.
  - [21] F. Pretorius, Phys. Rev. Lett. **95**, 121101 (2005), gr-qc/0507014.
  - [22] M. Campanelli, C. O. Lousto, P. Marronetti, and Y. Zlochower, Phys. Rev. Lett. **96**, 111101 (2006), gr-qc/0511048.
  - [23] J. G. Baker, J. Centrella, D.-I. Choi, M. Koppitz, and J. van Meter, Phys. Rev. Lett. **96**, 111102 (2006), gr-qc/0511103.
  - [24] C. V. Vishveshwara, Nature **227**, 936 (1970).
  - [25] C. V. Vishveshwara, Phys. Rev. D **1**, 2870 (1970).
  - [26] W. H. Press, Astrophys. J. Lett. **170**, L105 (1971).
  - [27] S. Chandrasekhar and S. L. Detweiler, Proc. Roy. Soc. Lond. A **344**, 441 (1975).
  - [28] S. L. Detweiler, Astrophys. J. **239**, 292 (1980).
  - [29] K. G. Arun, B. R. Iyer, M. S. S. Qusailah, and B. S. Sathyaprakash, Phys. Rev. D **74**, 024006 (2006), gr-qc/0604067.
  - [30] K. G. Arun, B. R. Iyer, M. S. S. Qusailah, and B. S. Sathyaprakash, Class. Quant. Grav. **23**, L37 (2006), gr-qc/0604018.
  - [31] M. Agathos, W. Del Pozzo, T. G. F. Li, C. Van Den Broeck, J. Veitch, and S. Vitale, Phys. Rev. D **89**, 082001 (2014), 1311.0420.
  - [32] B. P. Abbott et al. (LIGO Scientific, VIRGO), Phys. Rev. Lett. **118**, 221101 (2017), [Erratum: Phys.Rev.Lett. 121, 129901 (2018)], 1706.01812.
  - [33] A. Samajdar and K. G. Arun, Phys. Rev. D **96**, 104027 (2017), 1708.00671.
  - [34] B. P. Abbott et al. (LIGO Scientific, Virgo), Phys. Rev. Lett. **119**, 141101 (2017), 1709.09660.
  - [35] M. Isi and A. J. Weinstein (2017), 1710.03794.
  - [36] A. Ghosh et al., Phys. Rev. D **94**, 021101(R) (2016), 1602.02453.
  - [37] A. Ghosh, N. K. Johnson-Mcdaniel, A. Ghosh, C. K. Mishra, P. Ajith, W. Del Pozzo, C. P. Berry, A. B. Nielsen, and L. London, Class. Quant. Grav. **35**, 014002 (2018), 1704.06784.
  - [38] S. Ghonge, K. Chatzioannou, J. A. Clark, T. Littenberg, M. Millhouse, L. Cadonati, and N. Cornish (2020), 2003.09456.
  - [39] R. Abbott et al. (LIGO Scientific, Virgo), Phys. Rev. Lett. **125**, 101102 (2020), 2009.01075.
  - [40] R. Abbott et al. (LIGO Scientific, Virgo), Astrophys. J. Lett. **900**, L13 (2020), 2009.01190.
  - [41] W. Israel, Phys. Rev. **164**, 1776 (1967).
  - [42] S. W. Hawking, Commun. Math. Phys. **25**, 152 (1972).
  - [43] B. Carter, Phys. Rev. Lett. **26**, 331 (1971).
  - [44] D. C. Robinson, Phys. Rev. Lett. **34**, 905 (1975).
  - [45] P. O. Mazur, J. Phys. A **15**, 3173 (1982).

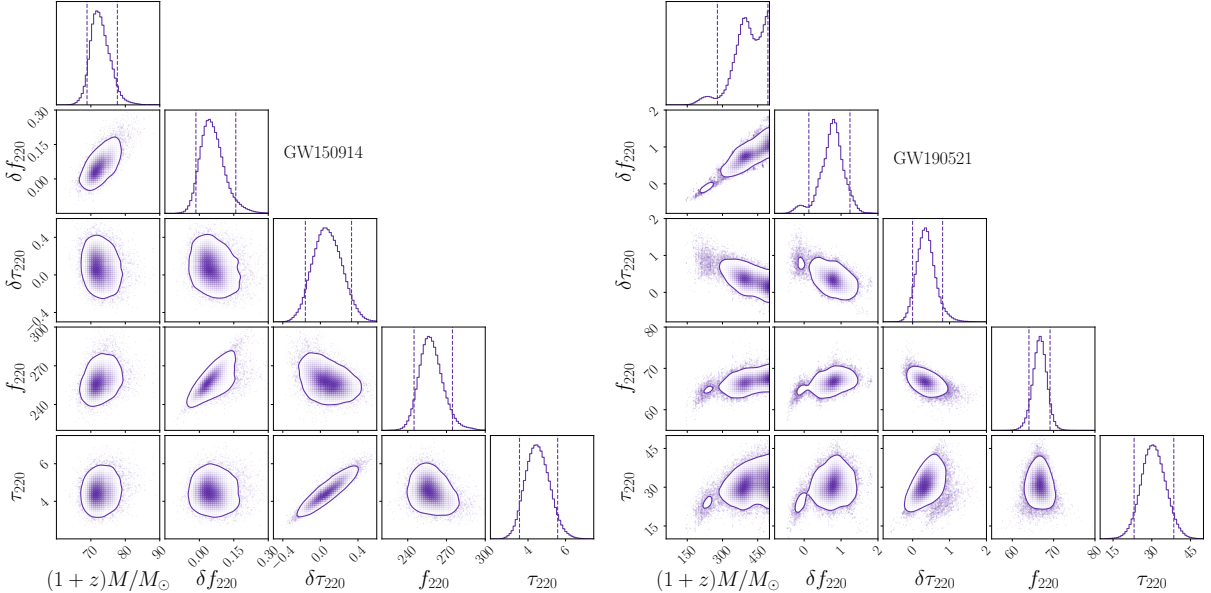


FIG. 8. Corner plots showing the correlations between the detector-frame total  $(1+z)M$ , the non-GR deviations  $(\delta f_{220}, \delta \tau_{220})$  and the reconstructed frequency and damping time  $(f_{220}, \tau_{220})$ . The left panel shows results for GW150914, for which  $\text{SNR} > 8$  in both the pre- and post-merger phase of the signal, and the correlations are absent. The right panel shows the results for GW190521, which has  $\text{SNR} > 8$  in the post-merger phase, but not in the pre-merger phase, and the correlations are present.

- [46] O. Dreyer, B. J. Kelly, B. Krishnan, L. S. Finn, D. Garrison, and R. Lopez-Aleman, *Class. Quant. Grav.* **21**, 787 (2004), gr-qc/0309007.
- [47] E. Berti, V. Cardoso, and C. M. Will, *Phys. Rev. D* **73**, 064030 (2006), gr-qc/0512160.
- [48] R. Brito, A. Buonanno, and V. Raymond, *Phys. Rev. D* **98**, 084038 (2018), 1805.00293.
- [49] G. Carullo, W. Del Pozzo, and J. Veitch, *Phys. Rev. D* **99**, 123029 (2019), [Erratum: *Phys. Rev. D* 100, 089903 (2019)], 1902.07527.
- [50] M. Isi, M. Giesler, W. M. Farr, M. A. Scheel, and S. A. Teukolsky, *Phys. Rev. Lett.* **123**, 111102 (2019), 1905.00869.
- [51] J. Calderón Bustillo, P. D. Lasky, and E. Thrane, *Phys. Rev. D* **103**, 024041 (2021), 2010.01857.
- [52] M. Giesler, M. Isi, M. A. Scheel, and S. Teukolsky, *Phys. Rev. X* **9**, 041060 (2019), 1903.08284.
- [53] S. Gossan, J. Veitch, and B. S. Sathyaprakash, *Phys. Rev. D* **85**, 124056 (2012), 1111.5819.
- [54] J. Meidam, M. Agathos, C. Van Den Broeck, J. Veitch, and B. S. Sathyaprakash, *Phys. Rev. D* **90**, 064009 (2014), 1406.3201.
- [55] G. Carullo et al., *Phys. Rev. D* **98**, 104020 (2018), 1805.04760.
- [56] G. Carullo, G. Riemschneider, K. W. Tsang, A. Nagar, and W. Del Pozzo, *Class. Quant. Grav.* **36**, 105009 (2019), 1811.08744.
- [57] S. Bhagwat, M. Cabero, C. D. Capano, B. Krishnan, and D. A. Brown, *Phys. Rev. D* **102**, 024023 (2020), 1910.13203.
- [58] M. Cabero, J. Westerweck, C. D. Capano, S. Kumar, A. B. Nielsen, and B. Krishnan, *Phys. Rev. D* **101**, 064044 (2020), 1911.01361.
- [59] A. Maselli, P. Pani, L. Gualtieri, and E. Berti, *Phys. Rev. D* **101**, 024043 (2020), 1910.12893.
- [60] M. Cabero, C. D. Capano, O. Fischer-Birnholtz, B. Krishnan, A. B. Nielsen, A. H. Nitz, and C. M. Biwer, *Phys. Rev. D* **97**, 124069 (2018), 1711.09073.
- [61] M. Isi, W. M. Farr, M. Giesler, M. A. Scheel, and S. A. Teukolsky (2020), 2012.04486.
- [62] G. Carullo, D. Laghi, J. Veitch, and W. Del Pozzo (2021), 2103.06167.
- [63] V. F. Foit and M. Kleban, *Class. Quant. Grav.* **36**, 035006 (2019), 1611.07009.
- [64] D. Laghi, G. Carullo, J. Veitch, and W. Del Pozzo (2020), 2011.03816.
- [65] A. B. Nielsen, C. D. Capano, O. Birnholtz, and J. Westerweck, *Phys. Rev. D* **99**, 104012 (2019), 1811.04904.
- [66] K. W. Tsang, A. Ghosh, A. Samajdar, K. Chatzioannou, S. Mastrogiannis, M. Agathos, and C. Van Den Broeck, *Phys. Rev. D* **101**, 064012 (2020), 1906.11168.
- [67] R. Lo, T. Li, and A. Weinstein, *Phys. Rev. D* **99**, 084052 (2019), 1811.07431.
- [68] J. Abedi and N. Afshordi, *JCAP* **11**, 010 (2019), 1803.10454.
- [69] J. Abedi and N. Afshordi (2020), 2001.00821.
- [70] A. Testa and P. Pani, *Phys. Rev. D* **98**, 044018 (2018), 1806.04253.
- [71] E. Berti, V. Cardoso, J. A. Gonzalez, U. Sperhake, M. Hannam, S. Husa, and B. Bruegmann, *Phys. Rev. D* **76**, 064034 (2007), gr-qc/0703053.
- [72] V. Baibhav, E. Berti, V. Cardoso, and G. Khanna, *Phys. Rev. D* **97**, 044048 (2018), 1710.02156.
- [73] S. Bhagwat, M. Okounkova, S. W. Ballmer, D. A. Brown, M. Giesler, M. A. Scheel, and S. A. Teukolsky, *Phys. Rev. D* **97**, 104065 (2018), 1711.00926.
- [74] A. Bohé et al., *Phys. Rev. D* **95**, 044028 (2017), 1611.03703.
- [75] A. Buonanno and T. Damour, *Phys. Rev. D* **59**, 084006 (1999), gr-qc/9811091.
- [76] A. Buonanno and T. Damour, *Phys. Rev. D* **62**, 064015 (2000), gr-qc/0001013.

- [77] R. Cotesta, A. Buonanno, A. Bohé, A. Taracchini, I. Hinder, and S. Ossokine, Phys. Rev. D **98**, 084028 (2018), 1803.10701.
- [78] E. Berti, V. Cardoso, and A. O. Starinets, Class. Quant. Grav. **26**, 163001 (2009), 0905.2975.
- [79] A. Taracchini et al., Phys. Rev. D **89**, 061502 (2014), 1311.2544.
- [80] F. Hofmann, E. Barausse, and L. Rezzolla, Astrophys. J. Lett. **825**, L19 (2016), 1605.01938.
- [81] N. Metropolis, A. W. Rosenbluth, M. N. Rosenbluth, A. H. Teller, and E. Teller, J. Chem. Phys. **21**, 1087 (1953).
- [82] W. K. Hastings, Biometrika **57**, 97 (1970).
- [83] J. Skilling, Bayesian Analysis **1**, 833 (2006).
- [84] J. Veitch et al., Phys. Rev. D **91**, 042003 (2015), 1409.7215.
- [85] G. Ashton et al., Astrophys. J. Suppl. **241**, 27 (2019), 1811.02042.
- [86] R. J. E. Smith, G. Ashton, A. Vajpeyi, and C. Talbot, Mon. Not. Roy. Astron. Soc. **498**, 4492 (2020), 1909.11873.
- [87] J. S. Speagle, Monthly Notices of the Royal Astronomical Society **493**, 3132–3158 (2020), ISSN 1365-2966, URL <http://dx.doi.org/10.1093/mnras/staa278>.
- [88] B. P. Abbott et al. (KAGRA, LIGO Scientific, Virgo), Living Rev. Rel. **23**, 3 (2020).
- [89] D. H. Shoemaker, Tech. Rep. LIGO-T1800044 (2010), <https://dcc.ligo.org/LIGO-T1800044/public>.
- [90] A. H. Mroue et al., Phys. Rev. Lett. **111**, 241104 (2013), 1304.6077.
- [91] H. Yang, K. Yagi, J. Blackman, L. Lehner, V. Paschalidis, F. Pretorius, and N. Yunes, Phys. Rev. Lett. **118**, 161101 (2017), 1701.05808.
- [92] A. Zimmerman, C.-J. Haster, and K. Chatzioannou, Phys. Rev. D **99**, 124044 (2019), 1903.11008.
- [93] M. Isi, K. Chatzioannou, and W. M. Farr, Phys. Rev. Lett. **123**, 121101 (2019), 1904.08011.
- [94] B. Carpenter, A. Gelman, M. D. Hoffman, D. Lee, B. Goodrich, M. Betancourt, M. Brubaker, J. Guo, P. Li, and A. Riddell, Journal of Statistical Software, Articles **76**, 1 (2017), ISSN 1548-7660.
- [95] G. Carullo (2021), 2102.05939.
- [96] K. Glampedakis and G. Pappas, Phys. Rev. D **97**, 041502 (2018), 1710.02136.
- [97] V. Cardoso and P. Pani, Living Rev. Rel. **22**, 4 (2019), 1904.05363.
- [98] E. Maggio, L. Buoninfante, A. Mazumdar, and P. Pani, Phys. Rev. D **102**, 064053 (2020), 2006.14628.
- [99] V. Ferrari, M. Pauri, and F. Piazza, Phys. Rev. D **63**, 064009 (2001), gr-qc/0005125.
- [100] C. Molina, P. Pani, V. Cardoso, and L. Gualtieri, Phys. Rev. D **81**, 124021 (2010), 1004.4007.
- [101] P. Pani and V. Cardoso, Phys. Rev. D **79**, 084031 (2009), 0902.1569.
- [102] J. L. Blázquez-Salcedo, C. F. B. Macedo, V. Cardoso, V. Ferrari, L. Gualtieri, F. S. Khoo, J. Kunz, and P. Pani, Phys. Rev. D **94**, 104024 (2016), 1609.01286.
- [103] J. L. Blázquez-Salcedo, F. S. Khoo, and J. Kunz, Phys. Rev. D **96**, 064008 (2017), 1706.03262.
- [104] R. Brito and C. Pacilio, Phys. Rev. D **98**, 104042 (2018), 1807.09081.
- [105] G. Franciolini, L. Hui, R. Penco, L. Santoni, and E. Trincherini, JHEP **02**, 127 (2019), 1810.07706.
- [106] V. Cardoso, M. Kimura, A. Maselli, and L. Senatore, Phys. Rev. Lett. **121**, 251105 (2018), 1808.08962.
- [107] O. J. Tattersall and P. G. Ferreira, Phys. Rev. D **97**, 104047 (2018), 1804.08950.
- [108] O. J. Tattersall, Class. Quant. Grav. **37**, 115007 (2020), 1911.07593.
- [109] J. L. Blázquez-Salcedo, S. Kahlen, and J. Kunz, Eur. Phys. J. C **79**, 1021 (2019), 1911.01943.
- [110] H. O. Silva and K. Glampedakis, Phys. Rev. D **101**, 044051 (2020), 1912.09286.
- [111] K. Glampedakis and H. O. Silva, Phys. Rev. D **100**, 044040 (2019), 1906.05455.
- [112] J. L. Blázquez-Salcedo, C. A. R. Herdeiro, S. Kahlen, J. Kunz, A. M. Pombo, and E. Radu (2020), 2008.11744.
- [113] J. L. Blázquez-Salcedo, D. D. Doneva, S. Kahlen, J. Kunz, P. Nedkova, and S. S. Yazadjiev, Phys. Rev. D **102**, 024086 (2020), 2006.06006.
- [114] P. A. Cano, K. Fransen, and T. Hertog, Phys. Rev. D **102**, 044047 (2020), 2005.03671.
- [115] P. K. Wagle, N. Yunes, and H. O. Silva (2021), 2103.09913.
- [116] L. Pierini and L. Gualtieri (2021), 2103.09870.
- [117] K. Glampedakis, G. Pappas, H. O. Silva, and E. Berti, Phys. Rev. D **96**, 064054 (2017), 1706.07658.
- [118] P. Jai-akson, A. Chatrabhuti, O. Evnin, and L. Lehner, Phys. Rev. D **96**, 044031 (2017), 1706.06519.
- [119] P. Pani, E. Berti, and L. Gualtieri, Phys. Rev. Lett. **110**, 241103 (2013), 1304.1160.
- [120] P. Pani, E. Berti, and L. Gualtieri, Phys. Rev. D **88**, 064048 (2013), 1307.7315.
- [121] Z. Mark, H. Yang, A. Zimmerman, and Y. Chen, Phys. Rev. D **91**, 044025 (2015), 1409.5800.
- [122] O. J. C. Dias, M. Godazgar, and J. E. Santos, Phys. Rev. Lett. **114**, 151101 (2015), 1501.04625.
- [123] M. Okounkova, L. C. Stein, M. A. Scheel, and S. A. Teukolsky, Phys. Rev. D **100**, 104026 (2019), 1906.08789.
- [124] M. Okounkova, L. C. Stein, J. Moxon, M. A. Scheel, and S. A. Teukolsky, Phys. Rev. D **101**, 104016 (2020), 1911.02588.
- [125] V. Cardoso, M. Kimura, A. Maselli, E. Berti, C. F. B. Macedo, and R. McManus, Phys. Rev. D **99**, 104077 (2019), 1901.01265.
- [126] R. McManus, E. Berti, C. F. B. Macedo, M. Kimura, A. Maselli, and V. Cardoso, Phys. Rev. D **100**, 044061 (2019), 1906.05155.
- [127] A. G. Suvorov and S. H. Völkel (2021), 2101.09697.
- [128] S. H. Völkel and E. Barausse, Phys. Rev. D **102**, 084025 (2020), 2007.02986.
- [129] S. H. Völkel, E. Barausse, N. Franchini, and A. E. Broderick (2020), 2011.06812.
- [130] D. Psaltis et al. (Event Horizon Telescope), Phys. Rev. Lett. **125**, 141104 (2020), 2010.01055.
- [131] H. Yang (2021), 2101.11129.
- [132] J. Healy, T. Bode, R. Haas, E. Pazos, P. Laguna, D. Shoemaker, and N. Yunes, Class. Quant. Grav. **29**, 232002 (2012), 1112.3928.
- [133] E. Berti, V. Cardoso, L. Gualtieri, M. Horbatsch, and U. Sperhake, Phys. Rev. D **87**, 124020 (2013), 1304.2836.
- [134] Z. Cao, P. Galaviz, and L.-F. Li, Phys. Rev. D **87**, 104029 (2013), 1608.07816.
- [135] M. Okounkova, L. C. Stein, M. A. Scheel, and D. A. Hemberger, Phys. Rev. D **96**, 044020 (2017), 1705.07924.
- [136] E. W. Hirschmann, L. Lehner, S. L. Liebling, and C. Palenzuela, Phys. Rev. D **97**, 064032 (2018), 1706.09875.
- [137] H. Witek, L. Gualtieri, P. Pani, and T. P. Sotiriou, Phys. Rev. D **99**, 064035 (2019), 1810.05177.
- [138] M. Okounkova (2020), 2001.03571.
- [139] W. E. East and J. L. Ripley (2020), 2011.03547.
- [140] S. Ossokine et al., Phys. Rev. D **102**, 044055 (2020), 2004.09442.